19e Journées de l'Hydrodynamique
26 – 28 novembre 2024, Nantes

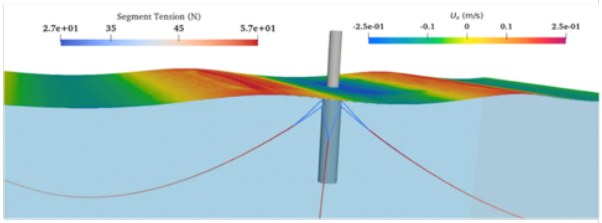

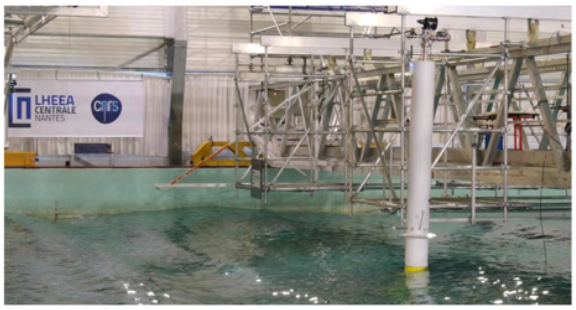

LES MESURES DE VELOCIMITRIE PAR IMAGERIE DE PARTICULES DES VAGUES PLONGEANTES

PARTICLE IMAGE VELOCIMETRY OF PLUNGING BREAKING WAVES

J. HARRIS[(1)], L. KIMMOUN[(2)], S. MOHANLAL[(3)], J. MCTIGHE[(4)], J. DAHL[(4)], S. GRILLI[(4)]

jeffrey.harris@enpc.fr ; s.mohanlal@hrwallingford.com ; jmctighe@uri.edu ; jmdahl@uri.edu ; grilli@uri.edu

[(1)]LHSV, Ecole des Ponts, EDF R&D, Chatou, France
[(2)]Centrale Marseille, IRPHE, France
[(3)]Coasts & Oceans, HR Wallingford, Wallingford, Oxfordshire, UK
[(4)]Department of Ocean Engineering, University of Rhode Island, Narragansett, RI, USA

Résumé

Des travaux récents sur les vagues déferlantes ont montré l'existence d'un critère de déferlement quasi-universel sur la base du facteur $B = u_{crête}/c_{crête}$, mais les résultats sont très sensibles aux valeurs des paramètres sélectionnés. Pour étudier cette question numériquement, nous appliquons une approche potentielle et complètement non-linéaire (FNPF) qui permet de reproduire précisément la surface libre, même lors du retournement qui précède le déferlement d'une vague. Des vagues plongeantes ont été générées dans le canal à houle de l'ECM, et la surface mesurée avec des jauges de vagues, tout en faisant des enregistrements vidéo à haute fréquence, qui permettent de faire des mesures de vélocimétrie par imagerie de particules (PIV). Ce système PIV permet de faire des observations très près de la crête des vagues, à l'instant de déferlement, de la vitesse du fluide, afin de valider les modèles. Ces mesures PIV sont analysées et comparées aux vitesses simulées du fluide ainsi qu'à la vitesse de phase.

Abstract

Recent works on breaking waves have shown a quasi-universal breaking criterion based on the ratio $B = u_{crest}/c_{crest}$, but the results are very sensitive to model parameters. To study this question numerially, we apply a fully nonlinear potential flow (FNPF) model that can reproduce precisely the free-surface movement, even after the overturning of a breaking wave. Plunging waves were generated in the ECM wave tank, and the surface measured with wave gauges and video, allowing for particle image velocimetry (PIV) analysis. This PIV system allows for observations of the fluid velocity close to the wave crest, at the moment of breaking, in order to validate model results. In this work, the PIV and FNPF results are compared in terms of fluid velocities and phase velocity.

I – Introduction

Offshore engineering is strongly affected by ocean waves, and in particular breaking waves that are associated with energy dissipation [2] or slamming loads on structures [11]. Despite the proliferation of different wave models, whether (among many others) Boussinesq, Serre-Green-Nagdhi, or fully nonlinear potential flow (FNPF), all different families models at handling the wave propagation and wave-structure interaction problem, breaking waves, depending on the fidelity of reproduction required, continue to be only approximately included. Whether based on hydraulic jump analogies [3], eddy viscosity models, or various turbulence models, they ultimately all require a breaking criterion to initiate the breaking event, and it is this aspect which has seen a lot of interest in recent years.

One breaking criterion that has become recently popular is the $B = u/c$ criterion of Barthelemy et al. [1], suggesting that a wave where the crest fluid velocity exceeds 0.85 times the crest phase velocity, would eventually overturn. A variety of works have looked at where this applies, including steepness or depth-limited breaking conditions, spilling or plunging conditions, and even 2D or 3D wave conditions. To date, only a few exceptions identified, such as by Scolan and Etienne [15] or Hasan et al. [6], have been found, so while mathematically it may not be a true universal criterion, it may be sufficient for most purposes. It is this breaking criterion that is considered in this paper. Further, work such as Derakhti et al. [2] showed that the time-derivative of the B parameter may be related to such things as the difference between spilling and breaking [12] or the slamming force on a structure [11]. Even of other breaking criteria that have been considered in the literature, a large question is understanding the crest kinematics.

One issue with the use of the B-criterion is that even though it appears before the overturning surface, it is sufficiently close to this event that high resolution may be required in order to capture the variation both of the exact crest position, but also the fluid velocity around the crest. In practice, if wave crest tracking is chosen for computing wave speed, and one may still need filtering in order to produce a consistent result, but this filtering may affect the result obtained. In some ways it is worth noting that this investigation of parameterizing breaking events is similar to earlier attempts by Longuet-Higgins [9] and numerous others who found analytic approximations to the crest flows.

At the same time, while FNPF theory is widely expected to be accurate up to the breaking moment, there is little experimental documentation of where this limit precisely is; certainly after the overturning wave hits the free-surface, viscous forces become important, but before then there may be questions of surface tension, varying air pressure, or other physics. Similar comparisons have been made previously to understand the performance of the Boussinesq wave equations for shoaling waves [14]. While breaking crest kinematics are used by many, there are quite few PIV measurements of these events, particularly those that trace quantities such as B over time [13].

In this paper, a comparison is made between PIV measurements of a focused wave and a BEM approach, to understand the errors associated to wave crest kinematics in plunging waves. First the experimental setup and test program is introduced, then the processing of the PIV data, for identifying the fluid velocity field and the free-surface identification. Next the FNPF solver, and associated simulations are presented, with matching wave-gauge records. Finally, a comparison of the crest properties and internal fluid kinematics between PIV and FNPF solver is given.

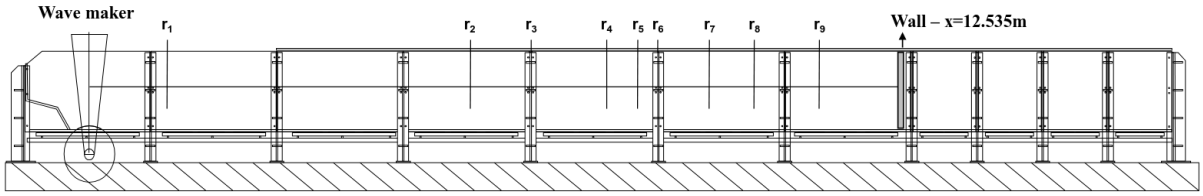

Figure 1: Setup of the physical wave flume, with breaking occuring near 8 m from the wavemaker, and wave gauges marked with black arrows.

II – Experimental setup

Experiments were performed at the wave flume of Ecole Centrale de Marseille (now known as Centrale Méditerranée), which in contrast to a conventional flap-type wavemaker, the axis of rotation is positioned $l = 0.4$ m below the bottom of the wave flume. The water depth for all experiments considered here was $h = 0.667$ m, and the far-wall is at a distance 12.535 m from the wavemaker (Fig. 1).

Within the wave flume, 6 resistive and 3 capacitive gauges were used to recored time-series of wave elevation (Table 1) with a sampling frequency of 300 Hz. Video was also recorded, for the purpose of PIV analysis of the breaking crests, similar to works like [7].

II – 1 Test conditions

Focused waves are generated by the wavemaker based on a discrete Ricker spectrum, commonly used in geophysics, and which was found by Kimmoun et al. [8] to limit high-frequency motion of the wavemaker that can induce errors and reduce the repeatability of experiments. This spectrum corresponds to the second derivative of the Gaussian function, with 2^{12} components given by:

$$s(\omega) = H\sqrt{T}e^{-\omega^m T}[1 - a(\omega^m T - 1)],\ a = \frac{1}{\omega_p^m T - 2} \tag{1}$$

where $\omega_p = 2\pi/T_p$ is the peak angular frequency, H is a design wave height, and m and T are spectral design parameters. This spectrum is also used in the works of [10] and [16].

Wave gauge	x-position (m)	Type
1	1.21	Resistive
2	5.91	Resistive
3	6.81	Resistive
4	8.03	Resistive
5	8.51	Resistive
6	8.83	Capacitive
7	9.62	Capacitive
8	10.30	Resistive
9	11.32	Capacitive

Table 1: Wave gauge location and type in the ECM wave flume (represented by arrows in Fig. 1).

Date	test	h (cm)	H_{max} (m)	X_{focal} (m)	dx (cm/px)	SL (px)
	8	66.7	0.2377	8	0.03188	
14-avr	9	66.7	0.2377	7.8	0.03188	920
	10	66.7	0.2377	7.6	0.03188	920
	11	66.7	0.2377	7.3	0.03188	920
	12	66.7	0.2485	7.4	0.03188	920
	13	66.7	0.2485	7.2	0.03188	920
	14	66.7	0.2485	7.2	0.03188	1915
15-avr	15	66.7	0.2485	7.2	0.03021	1915
	16	66.7	0.2485	7.5	0.03021	1915
	17	66.7	0.2593	7.5	0.03021	1915
	18	66.7	0.2593	7.2	0.03021	1915
	19	66.7	0.2593	7.8	0.03021	1915
	20	66.6	0.2593	7.5	0.016445	2480
	21	66.6	0.2593	7.2	0.016445	2480
	22	66.7	0.2593	7.2	0.016445	2480
	23	66.7	0.2593	7.8	0.016445	2480

Table 2: Test matrix of breaking wave tests conducted in 2021 at ECM, with tests 14, 15, and 19, discussed below, in gray. All tests were run with $T = 0.2285$, $m = 1.42$, and $T_p = 2.4\,\mathrm{s}$.

From this spectrum, the angular displacement of the flap is calculated as:

$$\theta(t) = \sum_j \frac{s(\omega_j)}{C(\omega_j)} \sin(\omega_j t - k_j x_f) d\omega \tag{2}$$

where x_f is the focusing distance from the wavemaker, k_j is the wave number calculated from the linear dispersion relation, $\omega_j = g k_j \tanh(k_j d)$, and $C(\omega)$ is the linear transfer function given by [8],

$$C(\omega) = \frac{2\sinh(kd)}{kd + \sinh(kd)\cosh(kd)} \left(\sinh(kd) + \frac{1 - \cosh(kd)}{k(d+l)} \right). \tag{3}$$

An example Ricker spectrum and its corresponding angular displacement are shown in Fig. 2.

Of the different tests in the test matrix (Table 2), we see that generally the height and focal distance was being adjusted to have the best view of the breaking crest in view of the PIV setup, and to verify repeatability. Due to the difficulty of separating the particle movement from the background noise (e.g., bright points in the air, reflections), we concentrate first on the question of repeatability between tests 14 and 15, next, then specifically the test 19 where the most results could be processed.

II – 2 Repeatability

In order to test the repeatability of the results, tests 14 and 15 were run with identical parameters, and we see quite similar evolution, both the time-series near the breaking point, and the evolution of the maximum wave evolution over the tank. Comparing two

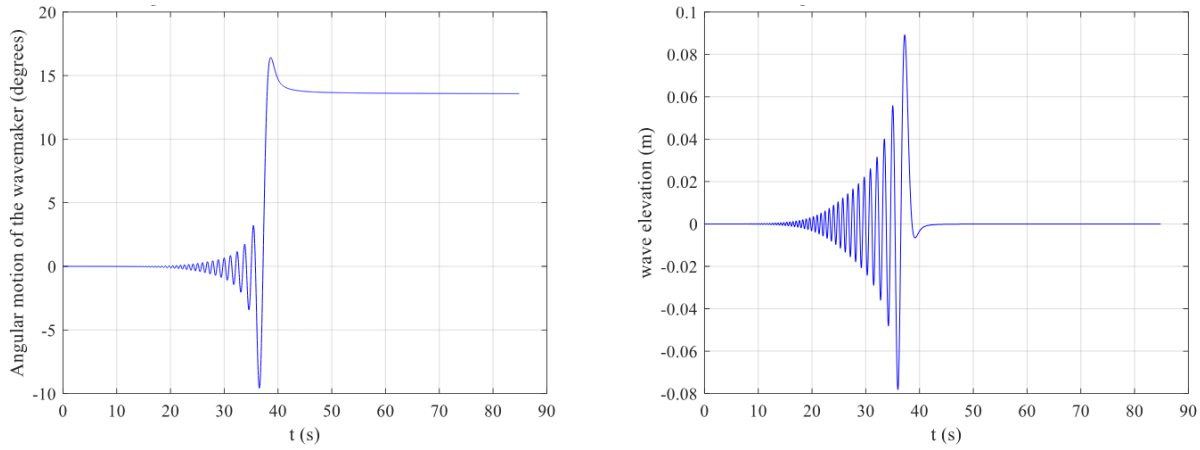

Figure 2: Example Ricker spectrum to illustrate the wavemaker motion (left) and linear estimation of generated focused wave elevation (right). Note that the time axis is shifted in comparison to the $t = 0$ of the numerical tests below.

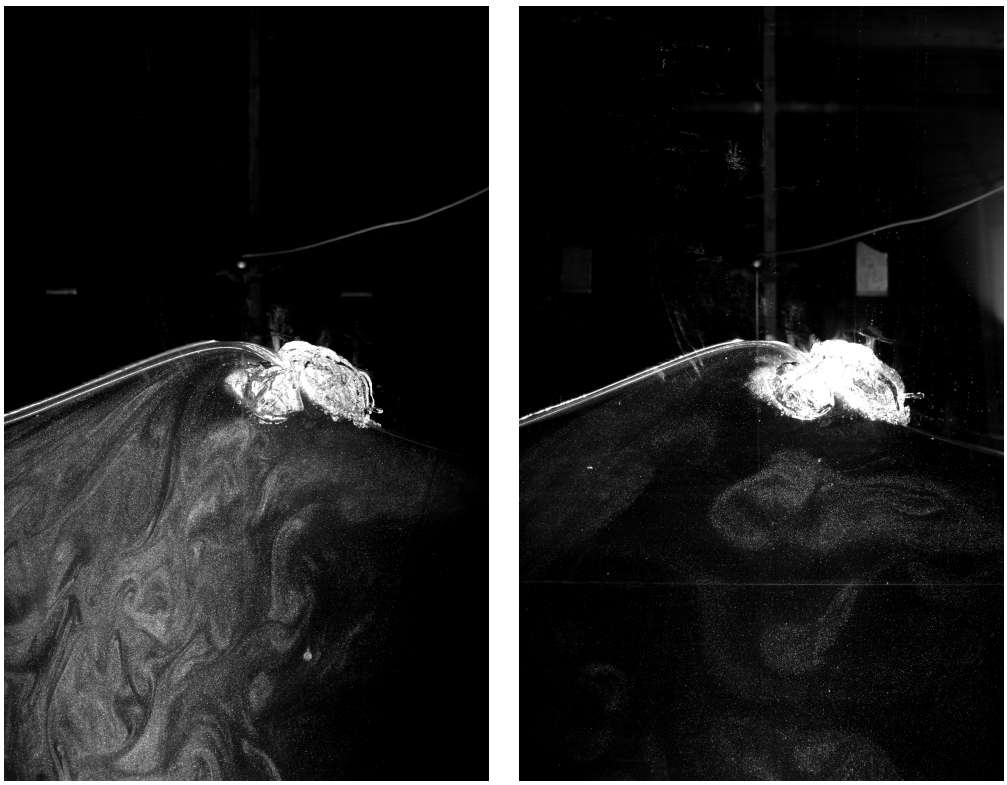

Figure 3: Comparison of test 14 and 15, showing the repeatability of the results; the visibility of the particles below the crest appear slightly different because the laser sheet was moved between the two tests, but otherwise the conditions are identical.

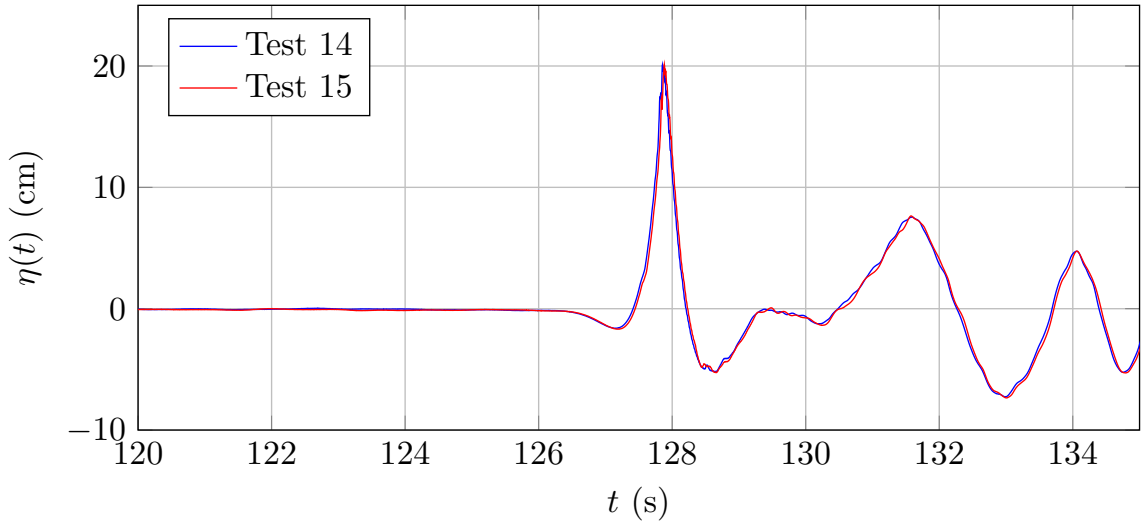

Figure 4: Comparison of tests 14 and 15, a priori the same, showing very similar time-series at $x = 8.03\,\mathrm{m}$ (wave gauge 4).

images, we see that indeed, there are slight differences in the shape of the broken wave (Fig. 3), but these are very slight and do not appear to affect the overall flow.

We can further establish the repeatability through the wave gauge measurements. Looking at a time-series of the gauge at the focal point (Fig. 4), we see nearly identical time-series, with a peak that is only 0.054 cm different (or 0.27% difference), with a time-shift of 0.028 s. Due to the similarity of some test runs, and the quality of the PIV images retained, we shall focus our attention for the rest of this paper on test 19, where the PIV data is more clear.

II – 3 PIV processing

The videos recorded from the experiments were processed using the PIVMat v4.20 software to extract fluid velocities. As seen in Fig. 5, due to objects in the background (e.g., wave gauge 4), reflections or scattering off the free surface, etc., there is some noise in the vector field, particularly around the crest, but resulting data does cover the area around the breaking crest.

For each moment that the velocities were calculated, two snapshots from the video were used. Given the data available, 16 instances, from just before to moments after the breaking of the test 19 wave, were retained for further analysis.

Free surface In order to aid in PIV processing, the free-surface was manually identified and points outside of the water were removed from the processing. This free-surface position was further retained for comparison with the NWT results, although the free surface position after the wave starts to overturn may have reduced accuracy.

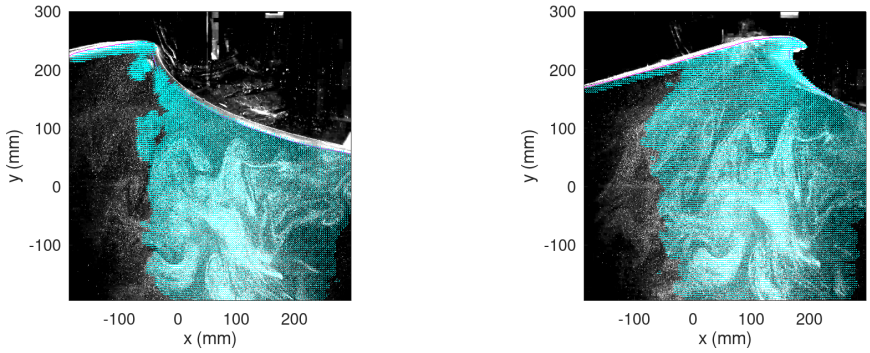

Figure 5: Two instants of test 19, both before (left) and after (right) the crest begins to overturn, with overlaid vectors corresponding to PIV calculated fluid velocity. The two instants are separated by 0.1 s.

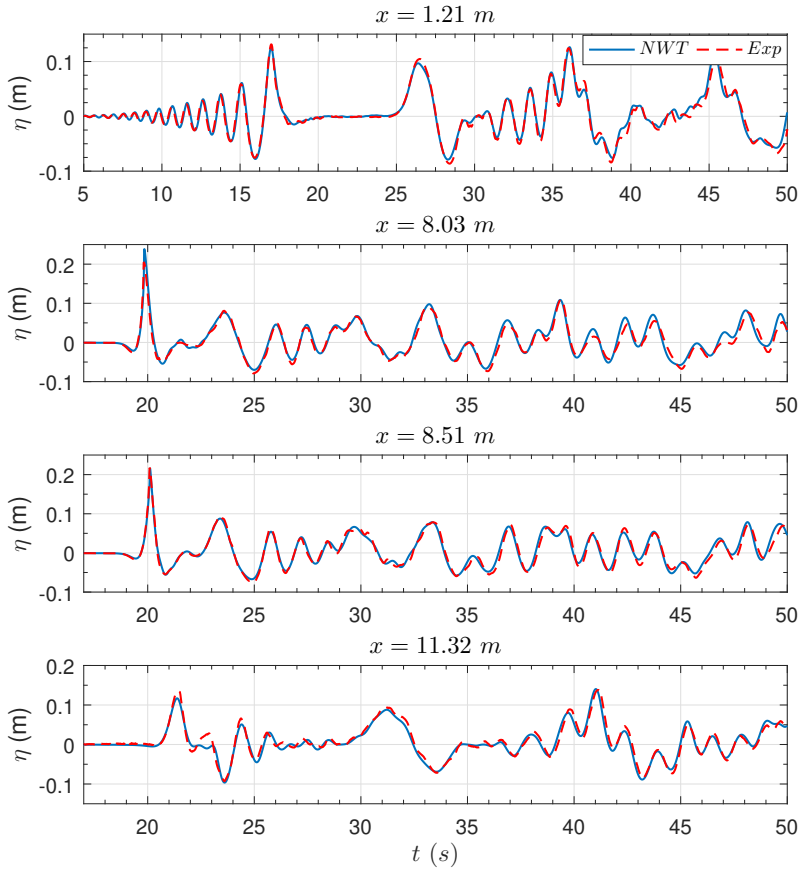

Figure 6: Time-series of experimental and numerical results of free-surface elevation for test 19 (including post-breaking, using the damping model as implemented in Mohanlal et al. [12]).

III – Numerical model

For comparison, the BEM code from Grilli et al. [4] and Grilli and Subramanya [5] is used, which is a FNPF solver, solving a Laplace equation,

$$\nabla^2 \phi = 0 \tag{4}$$

in the fluid domain Ω. For 2D flows, the kinematic and dynamic free surface boundary conditions can be written as:

$$\frac{Dr_i}{Dt} = \frac{\partial \phi}{\partial x_i} \tag{5}$$

$$\frac{D\phi}{Dt} = -gx_3 + \frac{1}{2}\frac{\partial \phi}{\partial x_i}\frac{\partial \phi}{\partial x_i} - \frac{p_a}{\rho}, \tag{6}$$

where x_3 is the vertical coordinate, and free-surface points are tracked in a Lagrangian way, and re-gridded regularly to maintain a relatively constant spacing.

To solve the Laplace equation, a boundary integral equation:

$$\alpha(x_j)\phi(x_j) = \int_\Gamma \left\{ \frac{\partial \phi(x_i)}{\partial n} G_{ij} - \phi(x_i)\frac{\partial G_{ij}}{\partial n} \right\} \mathrm{d}\Gamma(x_i), \tag{7}$$

with $G(x_i, x_j) = -\frac{1}{2\pi}\log|x_i - x_j|$. Numerical details can be found in the original works [4, 5].

Movement of the wavemaker is prescribed following the same expressions as the experimental wavemaker, an advantage of the boundary element approach. Like the experimental setup, no wave absorption is used. The model has been run both to consider the overturning wave (as in the work of Grilli et al. [4]), and with a damping pressure added (as in the work of Mohanlal et al. [12]), for comparing post-breaking time-series of elevation.

III – 1 Crest tracking

Given that the free-surface particles are being tracked already in the NWT, the crest is already available. Note that the free-surface is also being regrid every 3 time-steps, following the same procedures as Grilli and Subramanya [5];

In order to determine the crest phase velocity, following Mohanlal et al. [12], we use a local cubic interpolation to find the maximum in between two free-surface nodes, and find the time-derivative. A naive implementation is known to produce a noisy signal (as tracking a sub-grid maximum from one timestep to the next is with most models), so second-order exponential smoothing, as Mohanlal et al., is applied, and then the time-derivative is found over the previous 9 time-steps as a linear fit of the position.

III – 2 Internal velocities

The computation of internal velocity follows the same boundary integral procedure as above,

$$u_k(x_j) = \int_\Gamma \left\{ \frac{\partial \phi(x_i)}{\partial n}(\nabla_k G_{ij}) - \phi(x_i)\left(\nabla_k \frac{\partial G_{ij}}{\partial n}\right) \right\} \mathrm{d}\Gamma(x_i). \tag{8}$$

In order to match the PIV measurements, a set of fixed locations on a Cartesian grid are prescribed for calculating the internal velocity around the focal point of the wave.

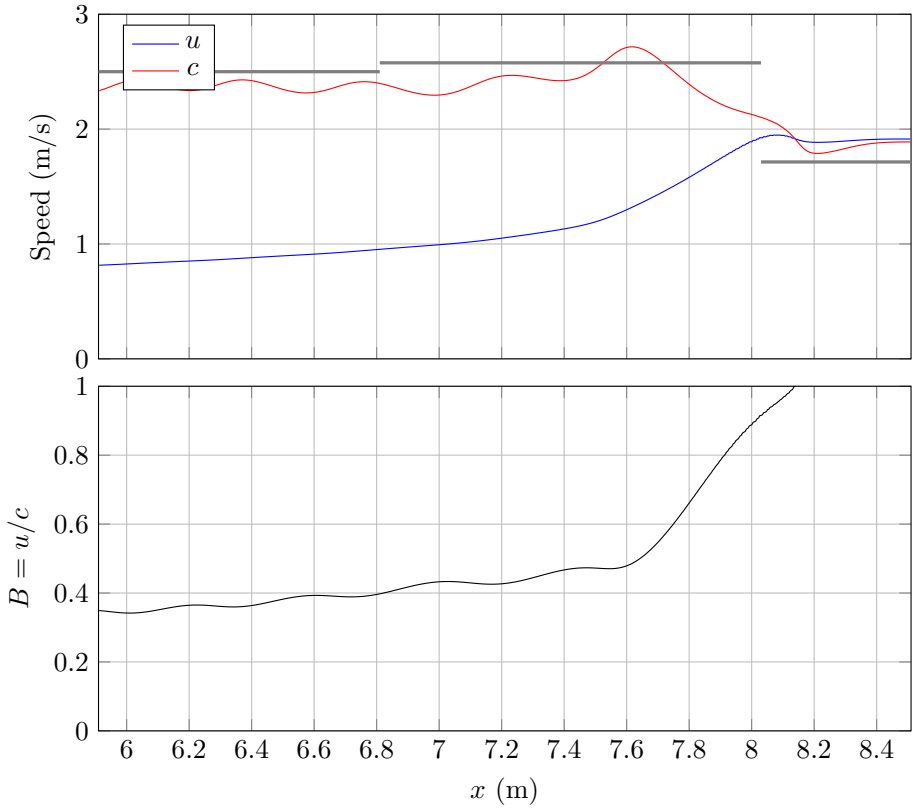

Figure 7: Plot of (upper) phase speed (c) and crest velocity (u) , and ratio $B = u/c$ (lower) as wave passes between wave gauges 2 and 5. Dashed lines indicate average phase speed estimated between wave gauges, using travel time between recorded peaks.

IV – Results

Crest tracking As the wave passes each wave gauge, noting the time and distance from the wavemaker is a first validation of the wave speed. In this sense (Fig. 7), the model and wave gauge data agrees well. As typical for breaking waves, the phase speed decreases just before a breaking event, and the crest velocity accelerates. Using the travel time between the elevation peaks at wave gauges 2, 3, 4, and 5, we are also able to check that the trend of phase speed is generally reasonable. The resulting wave speed and crest velocity then evolve to the breaking point, within the video field of view for PIV, analyzed next.

Free surface profile A critical point in the crest-tracking style of wave breaking is that the crest speed is correctly estimated. By matching the experimental and numerical positions around the point where the free-surface becomes vertical, we are able to match the free-surface elevation for some instants before and after breaking (Fig. 8). From this, we are able to see that, due to the numerical discretization, there match is imperfect, but the overall trend matches well between the two results. Further, using the crest tracking algorithm of Mohanlal et al., we are able to compute a speed of 2.159 m/s at the moment the $B = u/c = 0.85$ criterion is passed, which matches roughly the experimental result.

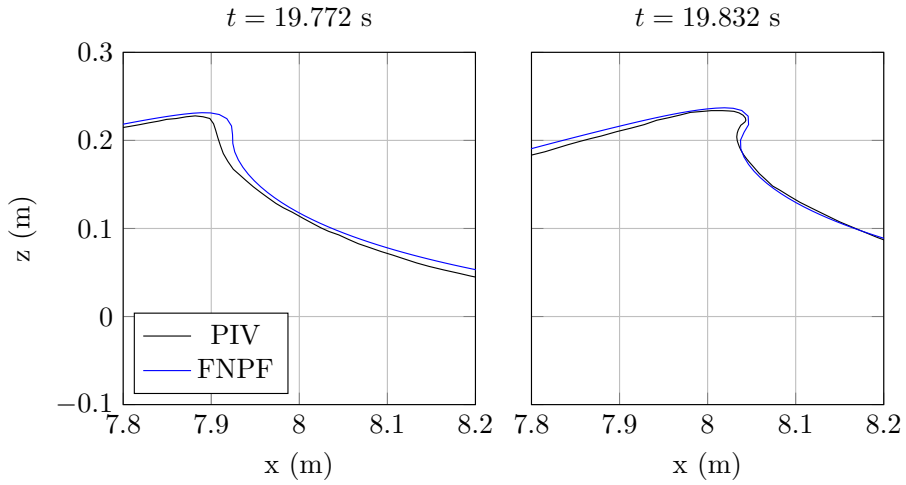

Figure 8: Comparison of wave elevation taken from manual analysis of experimental video (red) and FNPF result (black) for test 19.

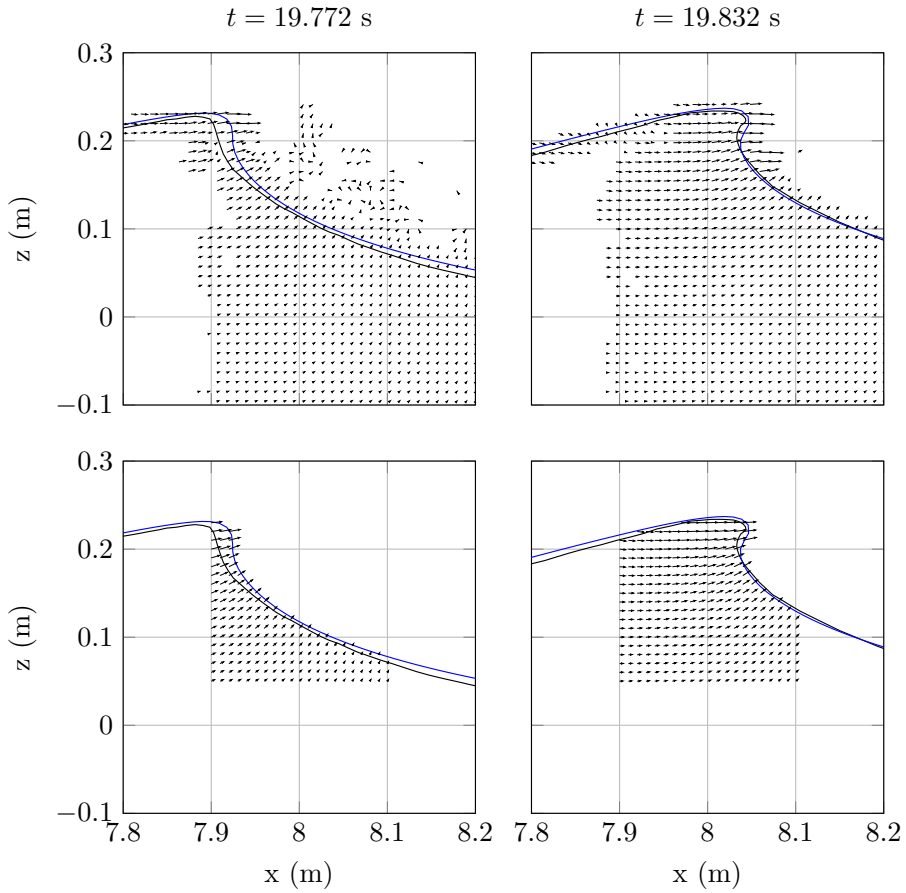

Figure 9: Comparison of PIV (upper) and FNPF (lower) results for test 19 wave just before (left) and after (right) wave overturning.

Fluid velocity comparison Plotting the fluid velocity, although the PIV result has some gaps or non-physical regions due to background noise, as well as some apparently velocities in the air from reflections and other artifacts, we are able to establish the overall pattern of fluid velocity around the breaking point (Fig. 9). Although this result is not at a high enough resolution to establish the exact value of u at the crest, it does match the overall trend of the FNPF result, suggesting that the numerical result is reasonable.

V – Conclusions

Experimentally produced focused plunging breaking waves in the ECM wave flume were measured with PIV, wave gauges. The use of a Ricker spectrum was chosen to aid reproducability, with wave height of the focused wave between two runs matching to within 0.5 mm.

A comparison between these results and a FNPF boundary element model shows good agreement of the free surface evolution, with similar crest phase velocities. While the fluid velocity at the crest is more difficult to measure, PIV of the internal fluid velocity also shows good agreement with the model results.

Given the interest of accurately predicting crest kinematics which may be related to a wave breaking criterion, impact forces on structures, or energy dissipation, further study of these results may prove to be a useful benchmark for numerical models that capture breaking events.

References

[1] X. Barthelemy, M. L. Banner, W. L. Peirson, F. Fedele, M. Allis, and F. Dias. On a unified breaking onset threshold for gravity waves in deep and intermediate depth water. *J. Fluid Mech.*, 841:463–488, 2018.

[2] M. Derakhti, M. L. Banner, and J. T. Kirby. Predicting the breaking strength of gravity water waves in deep and intermediate depth. *J. Fluid Mech.*, 848, 2018.

[3] S. T. Grilli, J. Horrillo, and S. Guignard. Fully nonlinear potential flow simulations of wave shoaling over slopes: Spilling breaker model and integral wave properties. *Water Waves*, 2:263–297, 2020.

[4] S. T. Grilli, J. Skourup, and I. Svendsen. An efficient boundary element method for nonlinear water waves. *Engng. Analysis with Boundary Elemts.*, 6(2):97–107, 1989.

[5] S. T. Grilli and R. Subramanya. Numerical modeling of wave breaking induced by fixed or moving boundaries. *Computational Mechanics*, 17(6):374–391, 1996.

[6] S. Hasan, V. Sriram, and R. P. Selvam. Evaluation of an eddy viscosity type wave breaking model for intermediate water depths. *European Journal of Mechanics-B/Fluids*, 78:115–138, 2019.

[7] O. Kimmoun and H. Branger. A particle image velocimetry investigation on laboratory surf-zone breaking waves over a sloping beach. *J. Fluid Mech.*, 588:353–397, 2007.

[8] O. Kimmoun, A. Ratouis, and L. Brosset. Sloshing and scaling: experimental study in a wave canal at two different scales. In *The Twentieth International Offshore and Polar Engineering Conference*. OnePetro, 2010.

[9] M. Longuet-Higgins. Parametric solutions for breaking waves. *Journal of Fluid Mechanics*, 121:403–424, 1982.

[10] P. Lubin, O. Kimmoun, F. Véron, and S. Glockner. Discussion on instabilities in breaking waves: vortices, air-entrainment and droplet generation. *European Journal of Mechanics-B/Fluids*, 73:144–156, 2019.

[11] M. B. Martin, J. C. Harris, J.-F. Filipot, F. Hulin, A. Tassin, and P. Renaud. Deep water focused breaking wave loads on a fixed cylinder. *Coastal Engng.*, 186:104397, 2023.

[12] S. Mohanlal, J. Harris, M. Yates, and S. Grilli. Unified depth-limited wave breaking detection and dissipation in fully nonlinear potential flow models. *Coastal Engng.*, 183:104316, 2023.

[13] B. Na, K.-A. Chang, and H.-J. Lim. Flow kinematics and air entrainment under laboratory spilling breaking waves. *Journal of Fluid Mechanics*, 882:A15, 2020.

[14] C. Narayanan and J. D. McCalpin. Vertical structure of horizontal velocity in regular shoaling waves. *Journal of Waterway, Port, Coastal, and Ocean Engineering*, 123(3):130–136, 1997.

[15] Y.-M. Scolan and S. Etienne. Pressure analysis in nonlinear waves by revisiting the breaking wave onset. *European Journal of Mechanics-B/Fluids*, 101:246–256, 2023.

[16] J. N. Steer, O. Kimmoun, and F. Dias. Breaking-wave induced pressure and acceleration on a clifftop boulder. *Journal of Fluid Mechanics*, 929:R1, 2021.